

Supporting Information

Bidirectional electron transfer boosts the Li-CO₂ electrochemistry

Pengfei Shu^a, Qiong Peng^{a,*}, Tingting Luo^a, Junfei Ding^a, Xiu Gong^a, Jian Zhou^b, Yadong Yu^c, Xiaosi Qi^{a,*} and Zhimei Sun^{b,*}

^a*College of Physics, Guizhou University, Guiyang 550025, China*

^b*School of Materials Science and Engineering, Beihang University, Beijing 100191, China*

^c*Institute of Chemical Defense, Academy of Military Science of the People's Liberation Army, Beijing 102205, China*

*E-mails: qpeng@gzu.edu.cn (Q. P.), xsqi@gzu.edu.cn (X. Q.), zmsun@buaa.edu.cn (Z. S.)

Table of Contents

S1. Supplementary figures obtained by constant charge method	2
S1.1. Effects of diverse CO ₂ adsorption configurations on the BET feature	2
S1.2. Structural stability of TM/Ti ₁₇ B ₁₈	5
S1.3. CO ₂ adsorption on TM/Ti ₁₇ B ₁₈	6
S1.4. Nucleation mechanisms of Li ₂ C ₂ O ₄ and Li ₂ CO ₃	7
S1.5. Discharge product dissociation mechanisms	10
S2. Supplementary tables obtained by constant charge method	13
S3. Supplementary results obtained by solvation and constant potential method	16
S3.1. Effects of solvation on the stability	16
S3.2. Constant potential effects	17
References	22

S1. Supplementary figures obtained by constant charge method

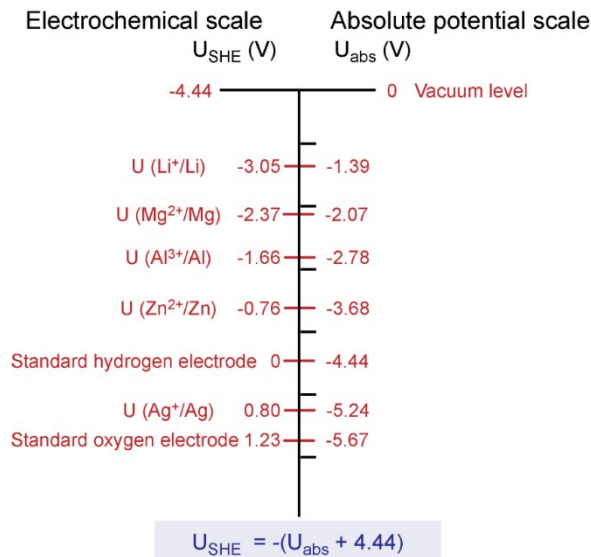


Fig. S1. The relation between the electrochemical potential and absolute potential.^{1, 2} For electrochemical potential U relative to Li⁺/Li, $U(\text{V vs. Li}^+/\text{Li}) = -1.39 - U_{\text{abs}}$.

S1.1. Effects of diverse CO₂ adsorption configurations on the BET feature

In terms of CO₂ adsorption on the TiB surface, the effects of diverse configurations on the bidirectional electron transfer (BET) behavior were taken into account. As seen in **Fig. S2**, the O atoms in CO₂ prefer to coordinate with four adjacent Ti atoms and are positioned above the bottom B sites. This configuration, featuring the most negative adsorption energy ($E_{\text{ads}} = -3.37$ eV), has been determined to be the thermodynamically optimal adsorption model. Notably, as the adsorption of CO₂ strengthens, the LDOS peak of the newly generated Ti d electron states becomes more prominent, particularly those located near -8 eV. This indicates that Ti active site can not only donate its occupied electrons to CO₂ empty antibonding orbitals, but also reversely capture the deep bonding electrons from CO₂ HOMO-1 orbitals, as further evidenced by the projected crystal orbital Hamilton population

(pCOHP). Such BET channel promotes the cleavage of C=O double bond and lowers the CO₂ bond order, thereby enhancing CO₂ activation and subsequent reduction.

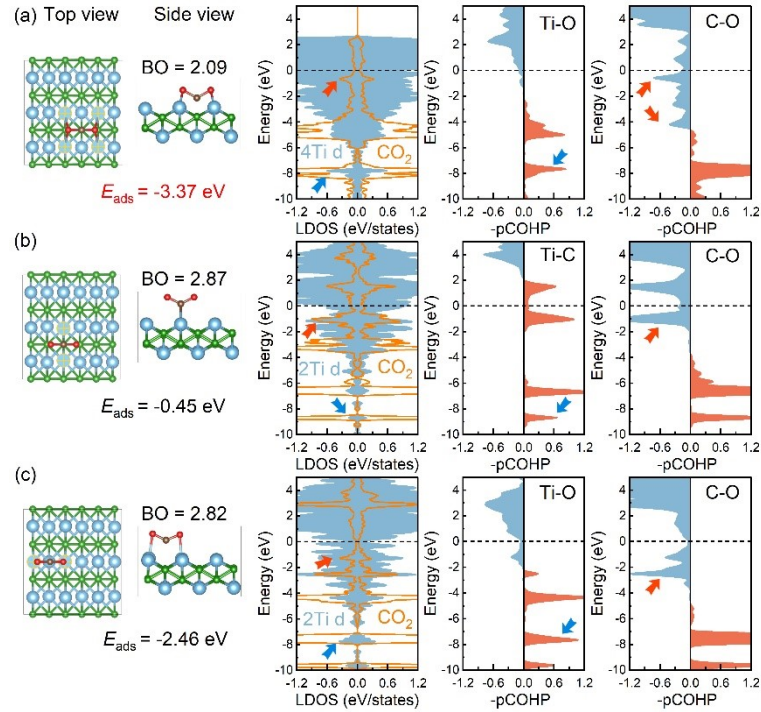


Fig. S2. Diverse configurations of CO₂ adsorption on the TiB surface, and corresponding adsorption energy E_{ads} , bond order (BO) of activated CO₂, as well as electronic properties. (a) O atoms coordinated with four Ti atoms and positioned above the bottom B sites, (b) C coordinated with two Ti atoms and O atoms located above the upper B sites, (c) O atoms coordinated with two Ti atoms and situated above the upper Ti sites. The green, blue, red and brown spheres represent B, Ti, O and C, respectively.

The charge density difference upon CO₂ adsorption was calculated as bellow:

$$\Delta\rho = \rho_{*\text{CO}_2} - \rho_* - \rho_{\text{CO}_2}$$

where the terms of $\rho_{*\text{CO}_2}$ and ρ_* represent the charge density of catalyst with and without adsorbing CO₂, and ρ_{CO_2} is the charge density of single CO₂ adsorbate.

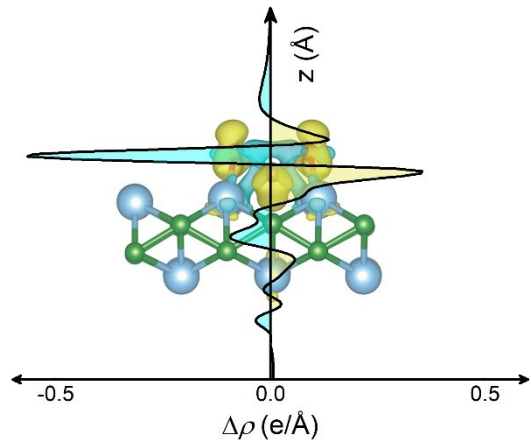


Fig. S3. Charge density difference for CO₂ adsorption on TiB, where the yellow and cyan indicate the charge accumulation and depletion, respectively.

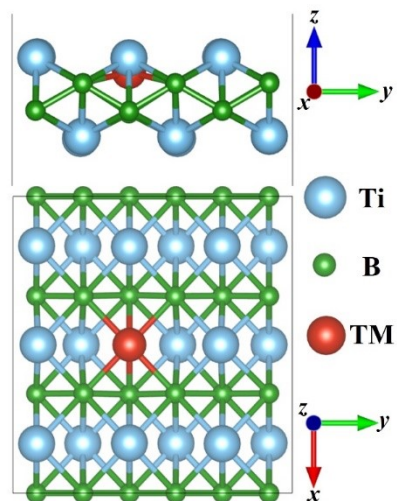


Fig. S4. Optimized configurations of 3d transition metal mediated TiB monolayer (TM/Ti₁₇B₁₈, TM = V, Cr, Mn, Fe, Co, Ni and Cu), where the surface Ti vacancy serves as the host for heterometal atoms.

S1.2. Structural stability of TM/Ti₁₇B₁₈

Whether the immobilized TM atoms would dissolve under electrochemical conditions, the dissolution potential (U_{diss} , vs SHE) was computed by implementing Eq. (S1) to provide further understanding the electrochemical stability of TM/Ti₁₇B₁₈ (TM = Ti, V, Cr, Mn, Fe, Co, Ni, Cu). Notably, the calculated U_{diss} values in **Table S1** are all greater than 0 V (vs. SHE), signifying these TM/Ti₁₇B₁₈ catalysts considered here are electrochemically stable.

$$U_{\text{diss}} = U_{\text{diss}}^0 - E_b / N_e. \quad (\text{S1})$$

where U_{diss}^0 and N_e refer to the standard electrode potential of bulk metal and the number of electrons transferred in the dissolution process, respectively. E_b represents the binding energy obtained from the following equation,

$$E_b = E_{\text{TM/Ti}_{17}\text{B}_{18}} - E_{\text{Ti}_{17}\text{B}_{18}} - E_{\text{TM}}^{\text{isolated}} \quad (\text{S2})$$

where $E_{\text{TM/Ti}_{17}\text{B}_{18}}$ and $E_{\text{Ti}_{17}\text{B}_{18}}$ denote the energies of TM/Ti₁₇B₁₈ composite and Ti₁₇B₁₈ substrate, respectively, and $E_{\text{TM}}^{\text{isolated}}$ is the energy of an isolated 3d transitional metal. A more negative E_b value denotes stronger adsorption of TM on the defective TiB substrate. In comparison with the cohesive energies of 3d bulk metals ($E_{\text{coh}} = E_{\text{TM}}^{\text{bulk}} / m - E_{\text{TM}}^{\text{isolated}}$, m represents the atomic number in the bulk metal), the resultant TM/Ti₁₇B₁₈ catalysts deliver much more negative binding energies, preventing anchored TM atoms from aggregating into clusters on the surfaces. The thermodynamic structural stability of TM/Ti₁₇B₁₈ was also confirmed by the negative formation energy E_f in **Fig. S5** with respect to the stable bulk metal, as described below:

$$E_f = E_{\text{TM/Ti}_{17}\text{B}_{18}} - E_{\text{Ti}_{17}\text{B}_{18}} - E_{\text{TM}}^{\text{bulk}}, \quad (\text{S3})$$

where $E_{\text{TM}}^{\text{bulk}}$ represents the total energy of the bulk metal.

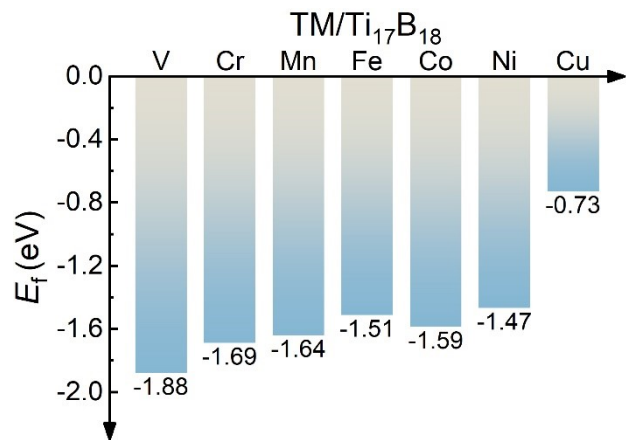


Fig. S5. The formation energy ($E_f = E_{\text{TM/Ti}_{17}\text{B}_{18}} - E_{\text{Ti}_{17}\text{B}_{18}} - E_{\text{TM}}^{\text{bulk}}$) of TM/Ti₁₇B₁₈ (TM = V, Cr, Mn, Fe, Co, Ni, Cu) relative to the stable bulk metal.

S1.3. CO₂ adsorption on TM/Ti₁₇B₁₈

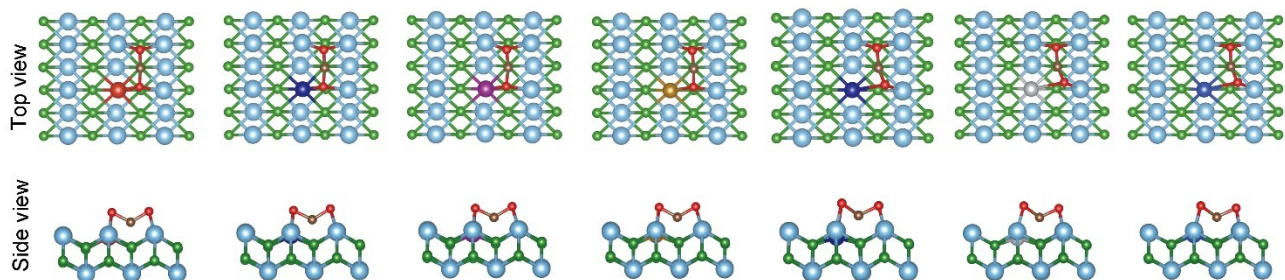


Fig. S6. Optimized CO₂ adsorption configurations on TM/Ti₁₇B₁₈ surface (TM = V, Cr, Mn, Fe, Co, Ni or Cu), where the blue, green, brown and red spheres represent Ti, B, C and O atoms, while the other colored spheres represent doped TM atoms.

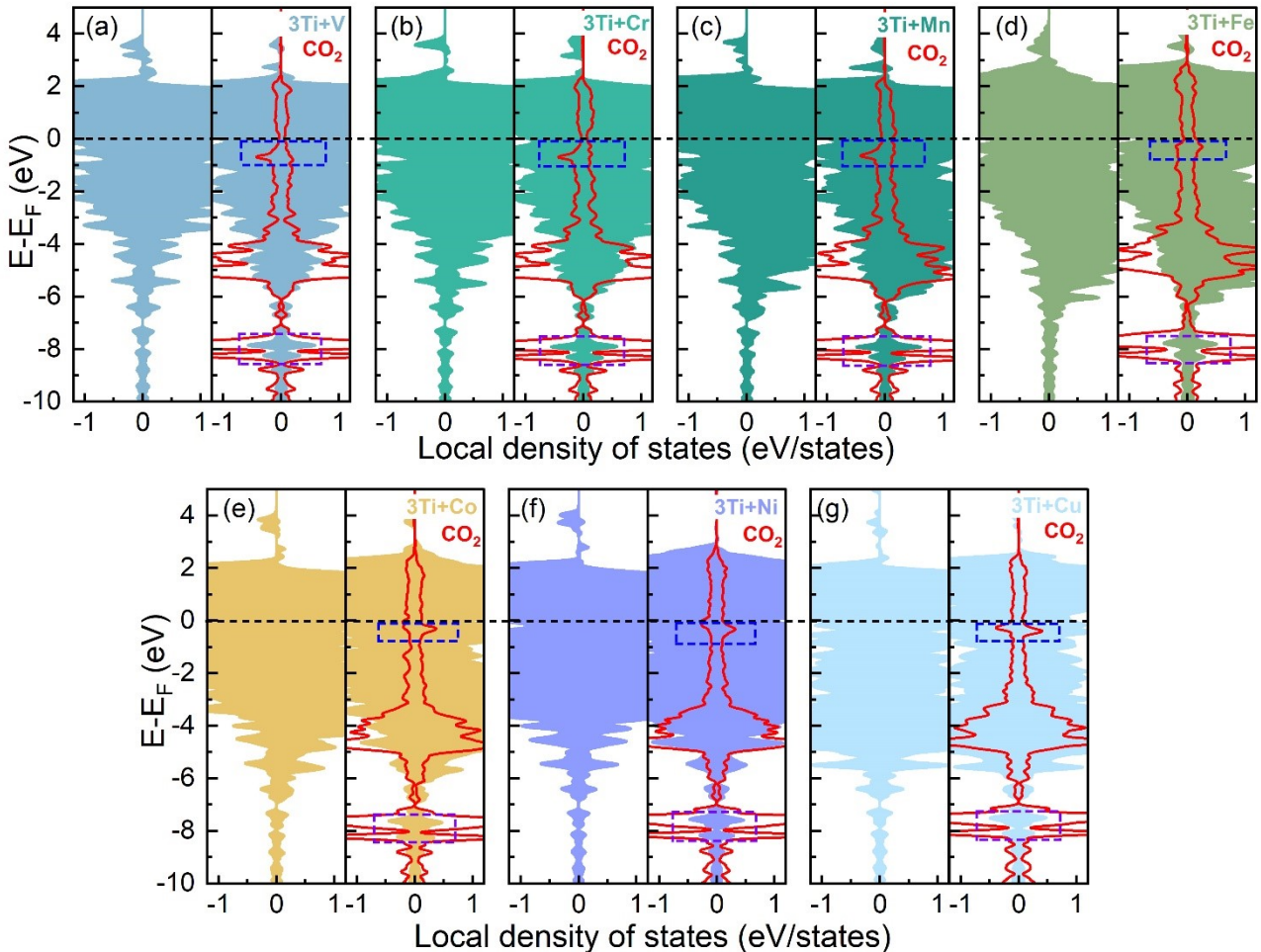


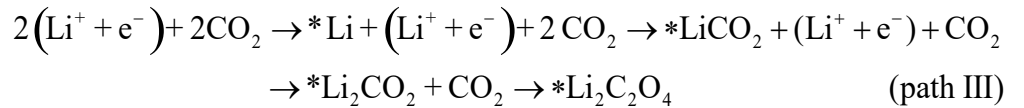
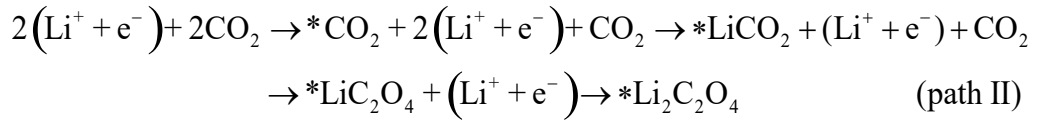
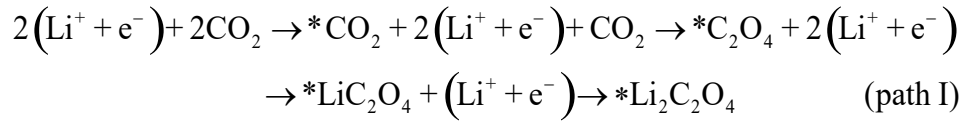
Fig. S7. Local density of states for activated CO_2 and d orbitals projected onto four adjacent metal atoms composed of $3\text{Ti} + \text{TM}$ directly bonded to CO_2 (right column) in comparison with bare $\text{TM/Ti}_{17}\text{B}_{18}$ ($\text{TM} = \text{V}, \text{Cr}, \text{Mn}, \text{Fe}, \text{Co}, \text{Ni}$ or Cu) (left column).

S1.4. Nucleation mechanisms of $\text{Li}_2\text{C}_2\text{O}_4$ and Li_2CO_3

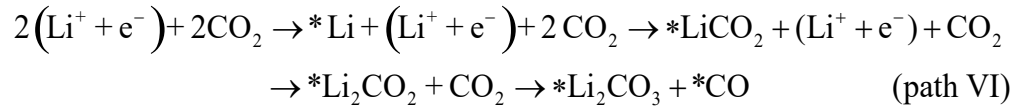
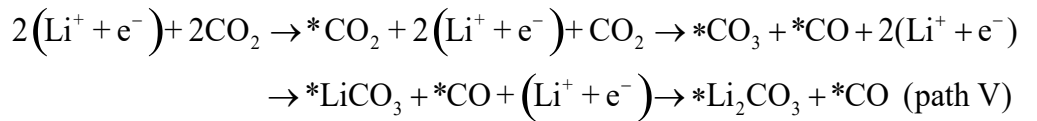
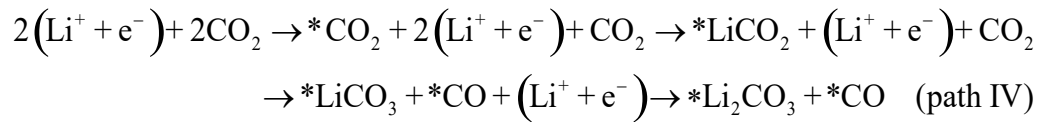
For aprotic Li-CO₂ batteries, the reversible electrochemical cathode reactions refer to $4\text{Li}^+ + 4\text{e}^- + 3\text{CO}_2(g) \rightleftharpoons \text{C} + 2\text{Li}_2\text{CO}_3$ via a four-electron transfer pathway.^{3, 4} The discharge process undergoes CO₂ reduction reaction (CO₂RR) to generate Li₂CO₃ and carbon products. However, based on recent experiments, *Li₂C₂O₄ intermediate was possibly formed at the beginning of discharge process, and even detected as final discharge product, as observed in Au and Mo₂C

catalyst surface.^{5, 6} In order to investigate the nucleation capacity of Li₂C₂O₄ and Li₂CO₃ in the presence of TM/Ti₁₇B₁₈ as catalysts, we examined several possible reaction pathways for the initial two electron transfer steps during discharging. Among them, paths I-III is Li₂C₂O₄ nucleation and paths IV-VI correspond to Li₂CO₃ nucleation, as shown below.^{5, 6}

(1) Li₂C₂O₄ nucleation:



(2) Li₂CO₃ nucleation:



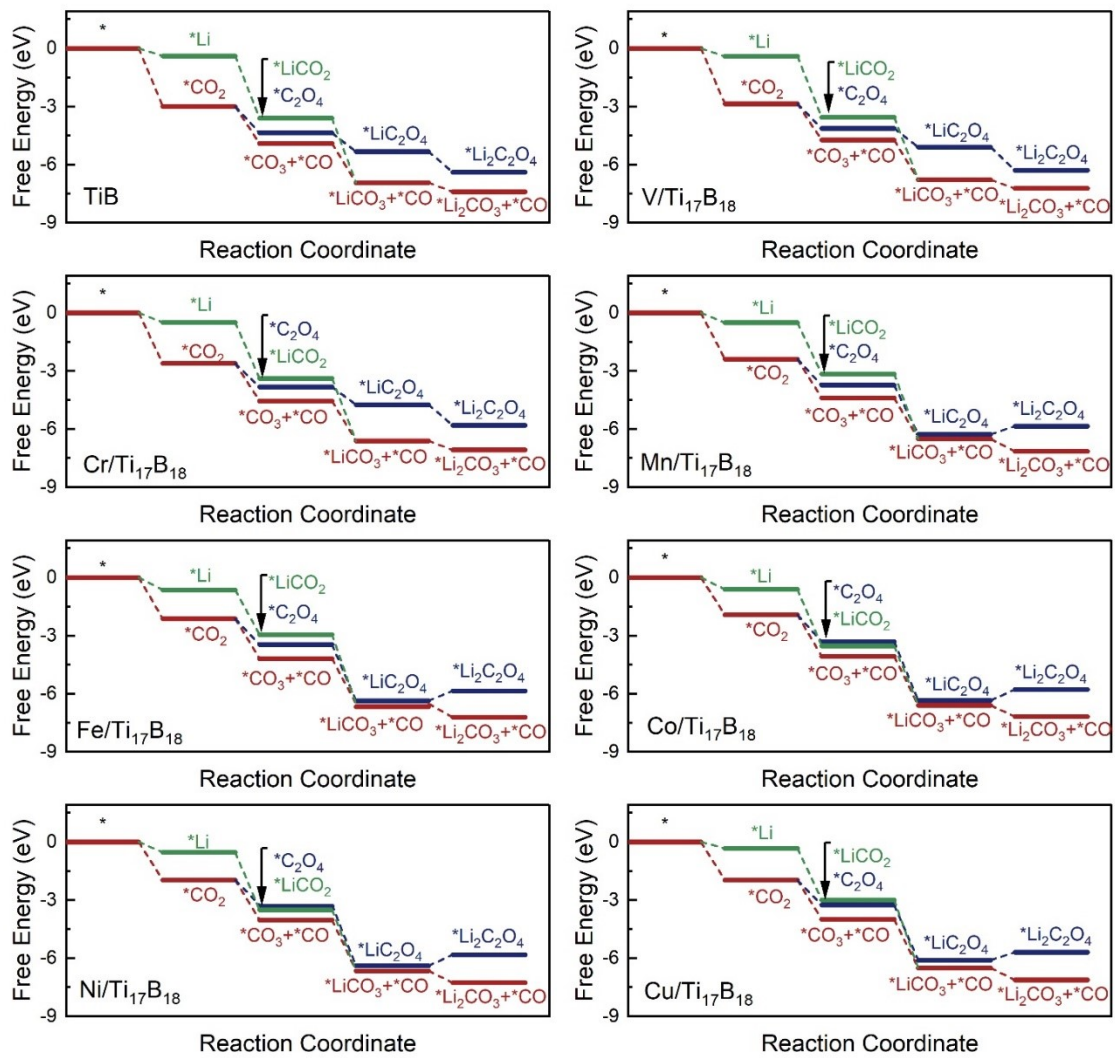
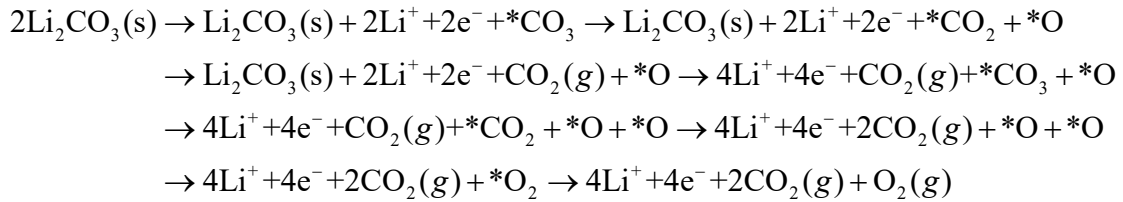


Fig. S8. Free energy profiles for the possible reaction pathways towards $*\text{Li}_2\text{C}_2\text{O}_4$ and $*\text{Li}_2\text{CO}_3$ nucleation at $\text{U} = 0 \text{ V}$ with TM/Ti₁₇B₁₈ as Li-CO₂ battery cathode catalysts.

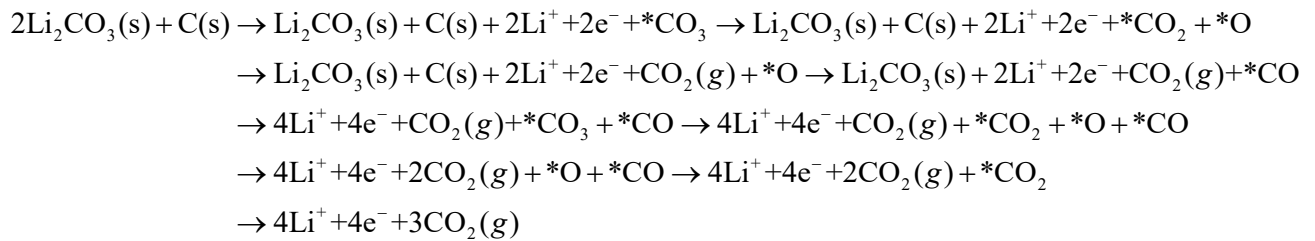
S1.5. Discharge product dissociation mechanisms

During the reverse charge process, CO₂ evolution reaction (CO₂ER) may exercise the individual decomposition of Li₂CO₃ ($2\text{Li}_2\text{CO}_3(\text{s}) \rightarrow 4\text{Li}^+ + 4\text{e}^- + 2\text{CO}_2(\text{g}) + \text{O}_2(\text{g})$) or co-decomposition with carbon products ($2\text{Li}_2\text{CO}_3(\text{s}) + \text{C}(\text{s}) \rightarrow 4\text{Li}^+ + 4\text{e}^- + 3\text{CO}_2(\text{g})$).⁷ Thus, these two possible decomposition mechanisms were further investigated in this work, as follows:

(1) The individual decomposition of Li₂CO₃:



(2) The co-oxidation decomposition of Li₂CO₃ and carbon:



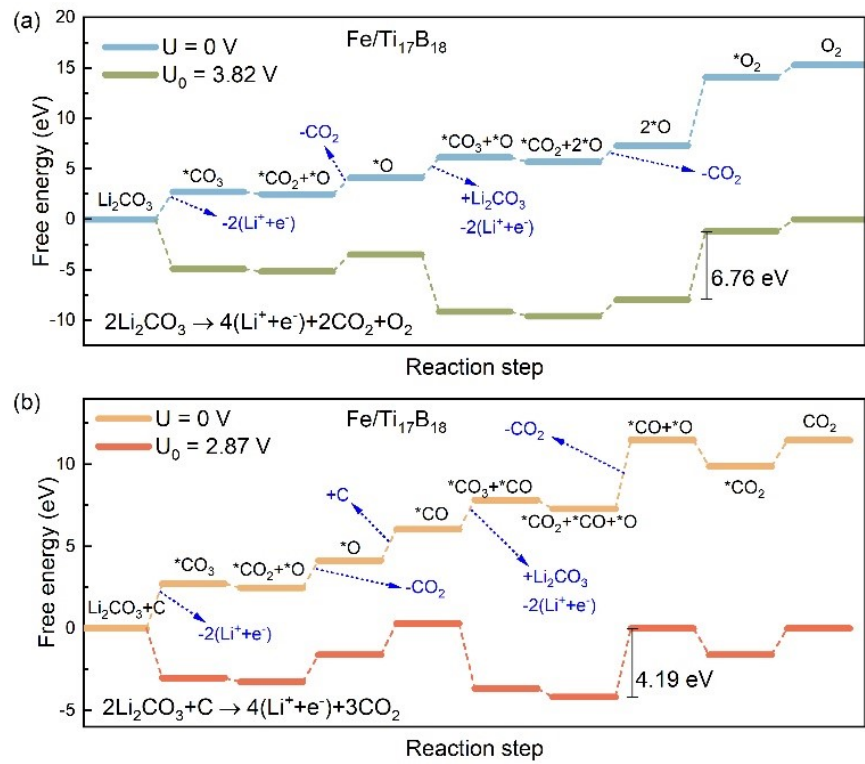


Fig. S9. Free energy diagrams for (a) the individual decomposition of Li_2CO_3 or (b) co-decomposition with carbon products on $\text{Fe}/\text{Ti}_{17}\text{B}_{18}$ catalyst.

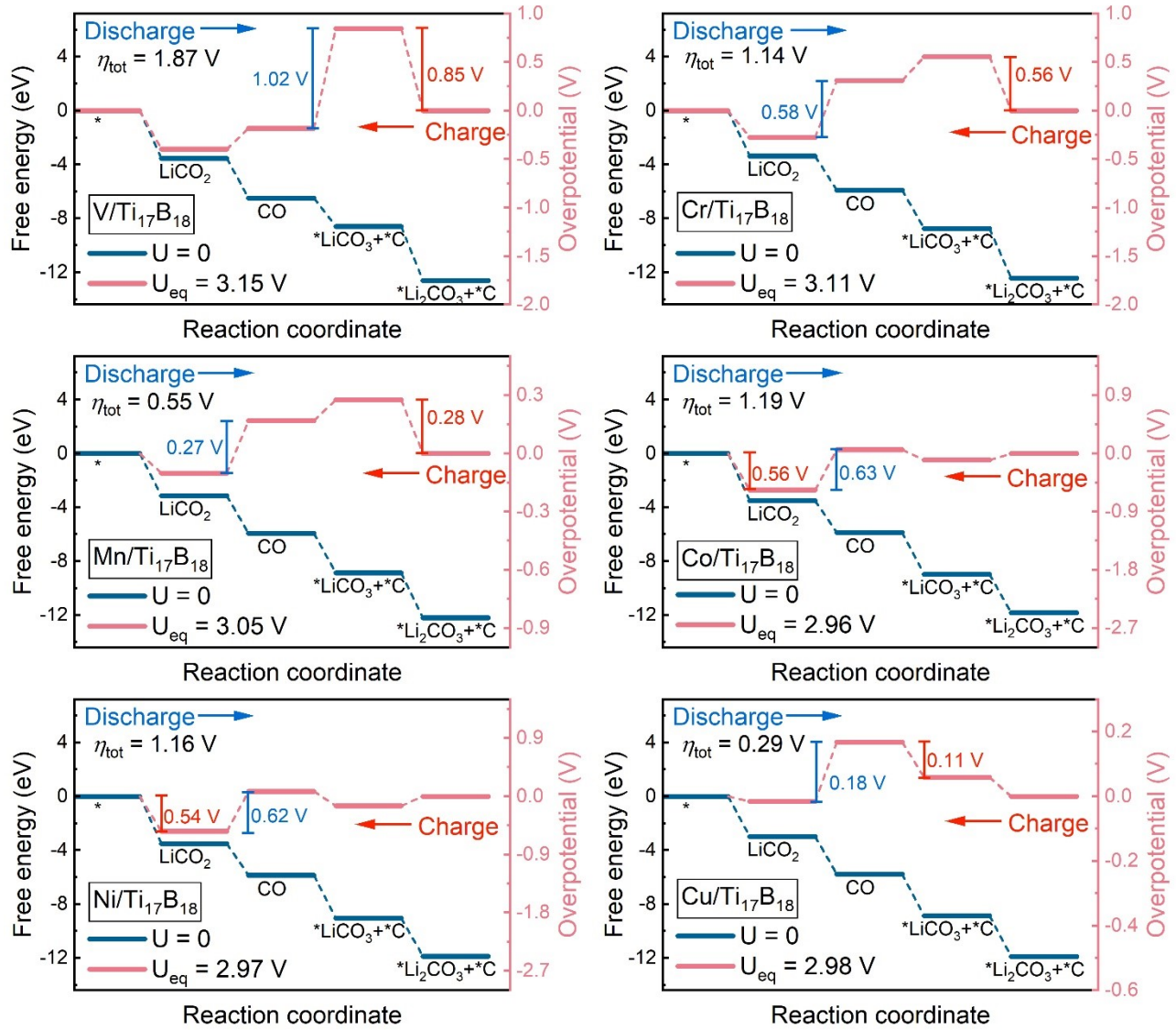


Fig. S10. Continuous four-electron transfer free energies on TM/ $\text{Ti}_{17}\text{B}_{18}$ catalysts, where blue and red numbers represent discharge overpotential (η_{DC}) and charge overpotential (η_{C}), respectively.

S2. Supplementary tables obtained by constant charge method

Table S1. U-J values used during the DFT+U calculations, cohesive energy of 3d transition metals (TM = Ti, V, Cr, Mn, Fe, Co, Ni, Cu), binding energy (E_b , eV) relative to isolated 3d metal, number of electrons (N_e) transferred during the dissolution, standard electrode potential (U_{diss}^0 , V vs. SHE) and computed dissolution potential (U_{diss} , V vs. SHE).

3d metal	Ti	V	Cr	Mn	Fe	Co	Ni	Cu
U-J	2.58	2.72	2.79	3.06	3.29	3.42	3.4	3.87
E_{coh}	-5.88	-5.95	-4.47	-4.11	-5.16	-5.64	-5.54	-3.99
E_b	-8.41	-7.83	-6.16	-5.75	-6.67	-7.20	-7.00	-4.72
N_e	3	2	3	2	2	2	2	2
U_{diss}^0	-1.37	-1.175	-0.74	-1.185	-0.44	-0.28	-0.25	+0.34
U_{diss}	1.43	2.74	1.31	1.69	2.90	3.32	3.25	2.70

Table S2. DFT energy E (eV) and chemical potential μ (V) of Li, CO₂, Li₂CO₃, CO and O₂.

Species	E	μ
Li	-	-1.99
CO ₂	-22.96	-23.12
Li ₂ CO ₃	-37.21	-40.01
CO	-14.77	-15.25
O ₂	-9.86	-9.94

Table S3. DFT total energy (E_{DFT}), zero-point energy (ΔE_{ZPE}) correction, entropy (S) and entropic contribution (TS, T = 298.15 K) to the Gibbs free energy.

Catalysts	Intermediates	E_{DFT} (eV)	ΔE_{ZPE} (eV)	S	TS (eV)
TiB	*	-273.59	-	-	-
	*LiCO ₂	-302.47	0.35	0.00059	0.18
	*CO	-290.32	0.19	0.00043	0.13
	*LiCO ₃ +*C	-317.61	0.58	0.00101	0.30
V/Ti ₁₇ B ₁₈	*Li ₂ CO ₃ +*C	-323.81	0.65	0.00121	0.36
	*	-274.18	-	-	-
	*LiCO ₂	-303.02	0.35	0.00058	0.17
	*CO	-290.94	0.19	0.00044	0.13
Cr/Ti ₁₇ B ₁₈	*LiCO ₃ +*C	-318.39	0.58	0.00104	0.31
	*Li ₂ CO ₃ +*C	-324.38	0.65	0.00125	0.37
	*	-274.43	-	-	-
	*LiCO ₂	-303.07	0.34	0.00064	0.19
Mn/Ti ₁₇ B ₁₈	*CO	-290.61	0.17	0.00020	0.06
	*LiCO ₃ +*C	-318.80	0.58	0.00098	0.29
	*Li ₂ CO ₃ +*C	-324.45	0.65	0.00123	0.37
	*	-273.69	-	-	-
Fe/Ti ₁₇ B ₁₈	*LiCO ₂	-302.09	0.34	0.00065	0.19
	*CO	289.92	0.18	0.00038	0.11
	*LiCO ₃ +*C	-318.17	0.58	0.00099	0.29
	*Li ₂ CO ₃ +*C	-323.54	0.65	0.00103	0.31
Co/Ti ₁₇ B ₁₈	*	-272.88	-	-	-
	*LiCO ₂	-301.06	0.33	0.00068	0.20
	*CO	289.06	0.18	0.00056	0.17
	*LiCO ₃ +*C	-317.46	0.58	0.00104	0.31
Ni/Ti ₁₇ B ₁₈	*Li ₂ CO ₃ +*C	-322.59	0.65	0.00122	0.36
	*	-271.77	-	-	-
	*LiCO ₂	-300.52	0.33	0.00073	0.22
	*CO	287.85	0.18	0.00058	0.17
	*LiCO ₃ +*C	-316.35	0.58	0.00101	0.30
	*Li ₂ CO ₃ +*C	-321.20	0.65	0.00120	0.36
	*	-270.16	-	-	-
	*LiCO ₂	-298.90	0.34	0.00072	0.21
	*CO	-286.28	0.18	0.00039	0.12
	*LiCO ₃ +*C	-314.79	0.58	0.00103	0.31
	*Li ₂ CO ₃ +*C	-319.62	0.65	0.00119	0.35

Catalysts	Intermediates	E_{DFT} (eV)	ΔE_{ZPE} (eV)	S	TS (eV)
	*	-267.79	-	-	-
	*LiCO ₂	-296.06	0.35	0.00061	0.18
Cu/Ti ₁₇ B ₁₈	*CO	-283.84	0.17	0.00039	0.12
	*LiCO ₃ +*C	-312.28	0.59	0.00095	0.28
	*Li ₂ CO ₃ +*C	-317.29	0.65	0.00118	0.35

Table S4. Bond order (BO) of activated CO₂ and the number of electrons transmitted in both directions ($\Delta\theta_- + \Delta\theta_+$), CO₂ adsorption energy ($E_{\text{ads}}^{\text{CO}_2}$, eV), LiCO₂ adsorption energy ($E_{\text{ads}}^{\text{LiCO}_2}$, eV), average C-O bond lengths of activated CO₂ ($l_{\text{C-O}}$, Å), ICOHP values, discharge overpotentials (η_{DC} , V), charge overpotentials (η_{C} , V) and total overpotentials (η_{tot} , V).

Catalysts	BO	$\Delta\theta_- + \Delta\theta_+$	$E_{\text{ads}}^{\text{CO}_2}$	$E_{\text{ads}}^{\text{LiCO}_2}$	$l_{\text{C-O}}$	ICOHP	η_{DC}	η_{C}	η_{tot}
TiB	2.09	3.82	-3.37	-3.93	1.37	-8.04	1.20	1.04	2.24
V/Ti ₁₇ B ₁₈	2.11	3.78	-3.24	-3.89	1.37	-7.82	1.02	0.85	1.87
Cr/Ti ₁₇ B ₁₈	2.15	3.70	-2.98	-3.69	1.36	-7.55	0.58	0.56	1.14
Mn/Ti ₁₇ B ₁₈	2.18	3.64	-2.73	-3.45	1.36	-7.14	0.27	0.28	0.55
Fe/Ti ₁₇ B ₁₈	2.23	3.54	-2.45	-3.23	1.35	-6.64	0.08	0.10	0.18
Co/Ti ₁₇ B ₁₈	2.25	3.50	-2.26	-3.80	1.35	-6.90	0.63	0.56	1.19
Ni/Ti ₁₇ B ₁₈	2.24	3.52	-2.31	-3.79	1.35	-6.92	0.62	0.54	1.16
Cu/Ti ₁₇ B ₁₈	2.21	3.59	-2.32	-3.33	1.36	-7.06	0.18	0.11	0.29

S3. Supplementary results obtained by solvation and constant potential method

S3.1. Effects of solvation on the stability

Ab initio molecular dynamics (AIMD) simulations were employed to explore the stability of 2D orthorhombic TiB monolayer under reaction conditions with ethylene carbonate (EC) serving as the aprotic solvent. **Fig. S11** shows the supercell for simulating the explicitly solvated TiB surface, which consists of 6×6 unit cells of TiB monolayer and 18 explicit $\text{C}_3\text{H}_4\text{O}_3$ molecules with a density of 1.32 g/cm³. Here, the AIMD calculations was carried out at 300 K for 10 ps using canonical NVT-ensemble with Nosé-Hoover thermostat,⁸ in which the time step was set to 2 fs. It is undeniable that the surface of TiB displays strong interactions with EC () solvent molecules, primarily ascribed to the presence of reactive carbonate groups () in EC. Alternatively, the utilization of other solvent molecules containing ether groups () is capable of effectively circumventing the intense interactions between the catalyst surface and solvent, such as tetraethylene glycol dimethyl ether (TEGDME, ) and dimethoxyethane (DME, ).^{9,10} This is an issue for future research to explore the effects of various solvent molecules on the CO_2 redox reaction. In this work, we focus on highlighting the BET mechanism to resolve the controversial issue of CO_2 activation on metal-based catalysts, and emphasizing its critical role in boosting the Li- CO_2 electrochemical performance.

Remarkably, throughout the last 10 ps during AIMD simulations, the temperature fluctuates slightly around 300K over time (**Fig. S11a**). Meanwhile, the structure of TiB does not undergo significant distortion and still maintains the basic configuration in comparison with original lattice (**Figs. S11b and S11c**). These results corroborate the outstanding structural tolerance and stability of TiB monolayer under reaction conditions without corrosion.

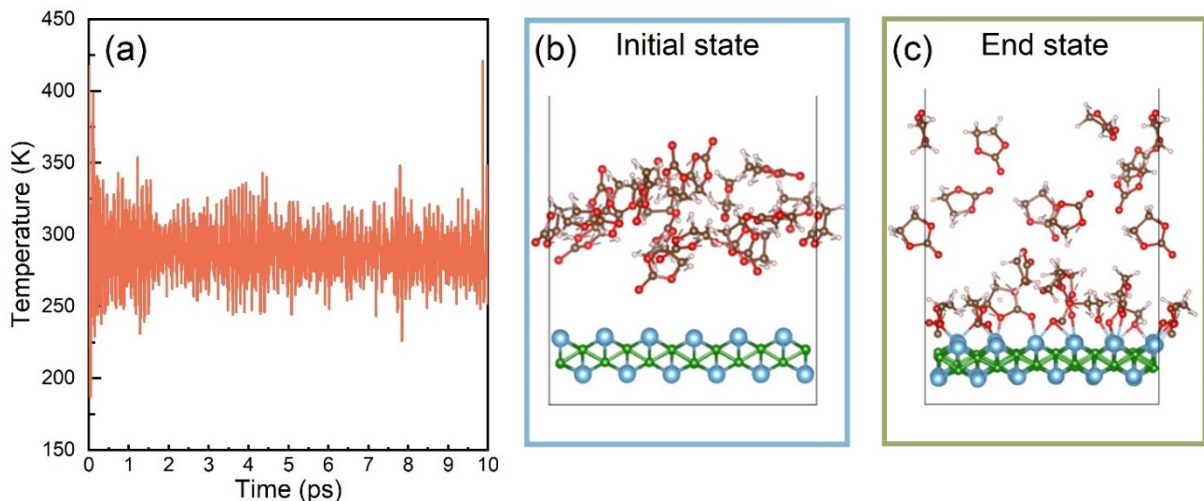


Fig. S11. (a) Temperature fluctuations versus the time (10 ps) for TiB monolayer in the explicit solvent model. (b,c) Comparative analysis of the atomic structure in TiB over time.

S3.2. Constant potential effects

To mimic realistic electrochemical conditions, we have implemented constant potential implicit solvation model to investigate the constant potential effects on the electronic structures of catalysts with and without adsorbates, especially on the BET mechanism, as well as their catalytic activity and selectivity for Li-CO₂ reaction. Using constant potential method (CPM) and taking Fe/Ti₁₇B₁₈ as a model catalyst, **Fig. S12** displays the coupling between the applied electrode potential and ionic charge distribution once CO₂ is adsorbed. The continuous distribution of ionic charge without voids demonstrates the rationality of the solvation parameter settings.¹¹ As a logical progression, the relation between energies and electrode potentials follows a quadratic function. For these TiB-based catalysts with implicit solvation effects, the energy and potential (vs. Li⁺/Li) do exhibit a quadratic parabolic relation by adding electrons ranging from -0.5e to +2e in 0.2e increments, but many abnormal points appear when removing electrons in the range of -2e to -0.5e. After excluding these outliers, we obtained the parabolic graph. The fitted parameters of capacitance (*C*), potential of zero charge (PZC),

and system energy at PZC are summarized in **Tables S5** and **S6**. It is seen that for TiB and Fe/Ti₁₇B₁₈, their PZC lies at 2.29 and 2.39 V vs. Li⁺/Li, and the surface area normalized capacitance is fitted to be 12.33 and 12.13 $\mu\text{F}/\text{cm}^2$ (expecting further experimental verification), respectively. This is close to that of Pt(111) surface ($C = 14 \mu\text{F}/\text{cm}^2$),¹² but only 58% of graphene ($C = 21 \mu\text{F}/\text{cm}^2$).¹³

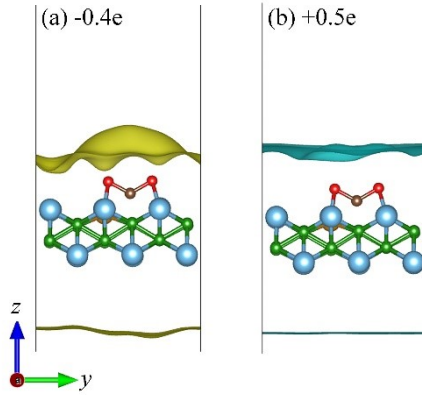


Fig. S12. Ionic charge density for CO₂ adsorption on Fe/Ti₁₇B₁₈ by (a) removing 0.4e and (b) adding 0.5e, where iso-surfaces is set to $1.4 \times 10^{-6} \text{ e}/\text{\AA}^{-3}$.

Table S5. For pristine TiB monolayer with/without intermediate adsorption, the fitted parameters of potential-dependent energy ($E = I + b1 \times U + b2 \times U^2$), potential of zero charge U_0 (V vs. Li⁺/Li), capacitance C_1 (e/V), and surface area normalized capacitance C_2 ($\mu\text{F}/\text{cm}^2$), system energy at potential of zero charge (E_0 , eV).

Species	I	b1	b2	C_1 (e/V)	C_2 ($\mu\text{F}/\text{cm}^2$)	U_0 (V)	E_0 (eV)	R^2
TiB	-274.696	1.475	-0.322	0.644	12.33	2.29	-273.01	0.9992
*CO ₂	-301.261	1.552	-0.330	0.661	12.67	2.35	-299.44	0.9998
*LiCO ₂	-303.731	1.082	-0.359	0.718	13.85	1.51	-302.92	0.9990
*CO	-291.733	1.583	-0.325	0.650	12.46	2.44	-289.80	0.9993
*LiCO ₃ +*C	-319.017	1.251	-0.369	0.738	14.16	1.70	-317.96	0.9996
*Li ₂ CO ₃ +*C	-325.179	0.997	-0.449	0.898	17.28	1.11	-324.63	0.9967

Table S6. For Fe/Ti₁₇B₁₈ with/without intermediate adsorption, the fitted parameters of potential-dependent energy ($E = I + b1 \times U + b2 \times U^2$), potential of zero charge U_0 (V vs. Li⁺/Li), capacitance C_1 (e/V), and surface area normalized capacitance C_2 ($\mu\text{F}/\text{cm}^2$), system energy at potential of zero charge (E_0 , eV).

Species	I	b1	b2	C_1 (e/V)	C_2 ($\mu\text{F}/\text{cm}^2$)	U_0 (V)	E_0 (eV)	R^2
Fe/Ti ₁₇ B ₁₈	-274.255	1.476	-0.311	0.622	12.13	2.37	-272.50	0.9996
*CO ₂	-299.801	1.573	-0.332	0.665	12.96	2.37	-297.94	0.9997
*LiCO ₂	-302.330	1.119	-0.350	0.700	13.60	1.60	-301.44	0.9970
*CO	-290.622	1.570	-0.318	0.636	12.40	2.47	-288.68	0.9999
*LiCO ₃ +*C	-318.861	1.381	-0.381	0.762	14.75	1.81	-317.61	0.9988
*Li ₂ CO ₃ +*C	-323.722	1.248	-0.520	1.040	20.01	1.20	-322.97	0.9945

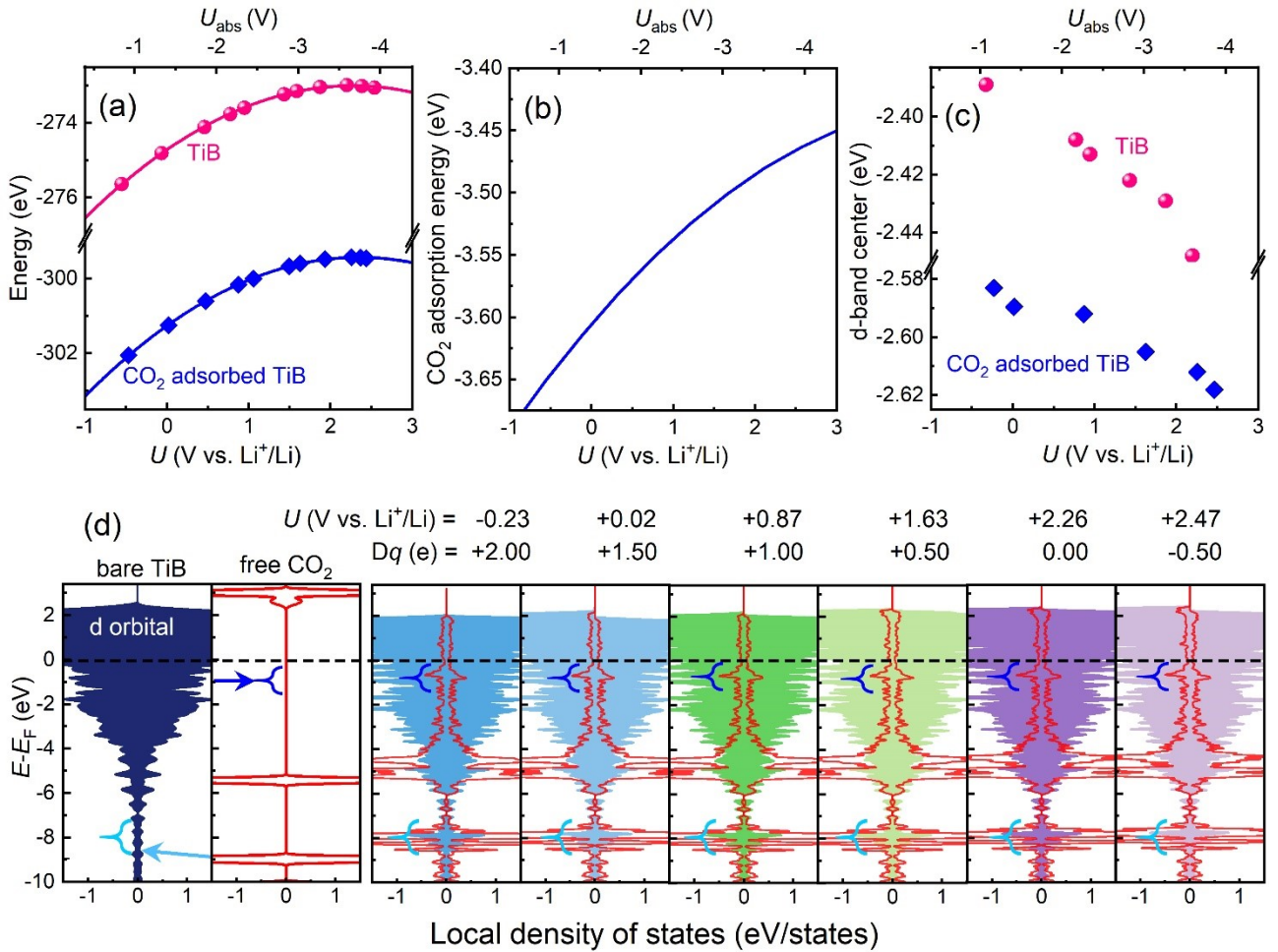


Fig. S13. (a) Calculated energies of TiB with/without CO_2 adsorption as a function of the electrode potential U vs. Li^+/Li . (b) Adsorption energies of $*\text{CO}_2$ on TiB. (c) The d band-center of bare TiB and CO_2 adsorbed TiB. (d) Local density of states for activated CO_2 (red lines) and d orbital (shaded region) projected on four adjacent metal atoms (4Ti) that directly bonded to CO_2 at various U vs. Li^+/Li .

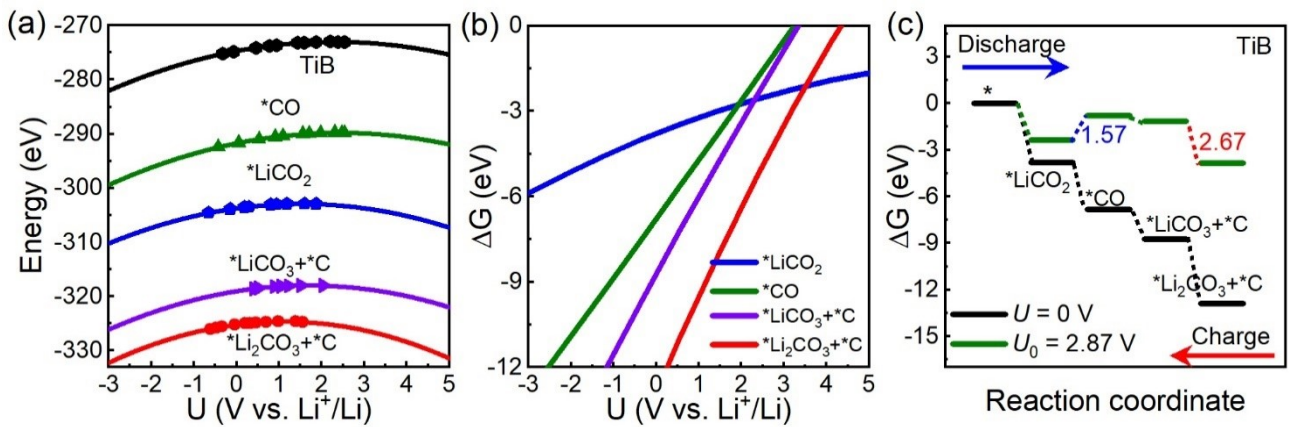


Fig. S14. (a) Calculated energies of pristine TiB with/without intermediate adsorption (*LiCO₂, *CO, *LiCO₃+*C and *Li₂CO₃ + *C) as a function of electrode potential U vs. Li⁺/Li. (b) Gibbs free energies of intermediate adsorption on TiB surface. (c) Continuous four-electron transfer free energy profiles with TiB as catalyst at U = 0 V and equilibrium potential of 2.87 V vs. Li⁺/Li.

References

1. S. Trasatti, *Pure Appl. Chem.*, 1986, **58**, 955-966.
2. Q. Zhang, Y. Zhang, S. Zhang and G. Gao, *J. Phys. Chem. C*, 2023, **127**, 16346-16356.
3. S. Xu, S. K. Das and L. A. Archer, *RSC Adv.*, 2013, **3**, 6656-6660.
4. X. Zhang, Y. Wang and Y. Li, *J. Phys. Chem. Lett.*, 2023, **14**, 1604-1608.
5. Y. Qiao, J. Yi, S. Wu, Y. Liu, S. Yang, P. He and H. Zhou, *Joule*, 2017, **1**, 359-370.
6. Y. Hou, J. Wang, L. Liu, Y. Liu, S. Chou, D. Shi, H. Liu, Y. Wu, W. Zhang and J. Chen, *Adv. Funct. Mater.*, 2017, **27**, 1700564.
7. J. Hu, C. Yang and K. Guo, *J. Mater. Chem. A*, 2022, **10**, 14028-14040.
8. S. Nosé, *J. Chem. Phys.*, 1984, **81**, 511-519.
9. X.-P. Zhang, Y.-N. Li, Y.-Y. Sun and T. Zhang, *Angew. Chem. Int. Ed.*, 2019, **58**, 18394-18398.
10. T. Chen, Z. Jin, Y. Liu, X. Zhang, H. Wu, M. Li, W. Feng, Q. Zhang and C. Wang, *Angew. Chem. Int. Ed.*, 2022, **61**, e202207645.
11. X. Hu, S. Chen, L. Chen, Y. Tian, S. Yao, Z. Lu, X. Zhang and Z. Zhou, *J. Am. Chem. Soc.*, 2022, **144**, 18144-18152.
12. K. Mathew, V. S. C. Kolluru, S. Mula, S. N. Steinmann and R. G. Hennig, *J. Chem. Phys.*, 2019, **151**, 234101.
13. J. Chen, C. Li and G. Shi, *J. Phys. Chem. Lett.*, 2013, **4**, 1244-1253.